Energy capture and storage in asymmetrically multistable modular structures inspired by skeletal muscle

You may also be interested in:

Investigation of a bistable dual-stage vibration isolator under harmonic excitation
Kai Yang, R L Harne, K W Wang et al.

Structure–function relationship of skeletal muscle provides inspiration for design of new artificial muscle
Yingxin Gao and Chi Zhang

A review of the recent research on vibration energy harvesting via bistable systems
R L Harne and K W Wang

The pull-in behavior of electrostatically actuated bistable microstructures
Slava Krylov, Bojan R Ilic, David Schreiber et al.

Enhancement of quasi-static strain energy harvesters using non-uniform cross-section post-buckled beams
Pengcheng Jiao, Wassim Borchani, Hassene Hasni et al.

A concept for energy harvesting from quasi-static structural deformations through axially loaded bilaterally constrained columns with multiple bifurcation points
N Lajnef, R Burgueño, W Borchani et al.

Effect of large deformation pre-loads on the wave properties of hexagonal lattices
Raj Kumar Pal, Julian Rimoli and Massimo Ruzzene

A new hysteresis model based on force–displacement characteristics of magnetorheological fluid actuators subjected to squeeze mode operation
Peng Chen, Xian-Xu Bai, Li-Jun Qian et al.

Energy capture and storage in asymmetrically multistable modular structures inspired by skeletal muscle

Narayanan Kidambi[1,3]**, Ryan L Harne**[2] **and K W Wang**[1]

[1] Department of Mechanical Engineering, University of Michigan, Ann Arbor, MI 48109, United States of America
[2] Department of Mechanical and Aerospace Engineering, The Ohio State University, Columbus, OH 43210, United States of America

E-mail: kidambi@umich.edu

CrossMark

Abstract

The remarkable versatility and adaptability of skeletal muscle that arises from the assembly of its nanoscale cross-bridges into micro-scale assemblies known as sarcomeres provides great inspiration for the development of advanced adaptive structures and material systems. Motivated by the capability of cross-bridges to capture elastic strain energy to improve the energetic efficiency of sudden movements and repeated motions, and by models of cross-bridge power stroke motions and sarcomere contractile behaviors that incorporate asymmetric, bistable potential energy landscapes, this research develops and studies modular mechanical structures that trap and store energy in higher-energy configurations. Modules exhibiting tailorable asymmetric bistability are first designed and fabricated, revealing how geometric parameters influence the asymmetry of the resulting double-well energy landscapes. These experimentally-observed characteristics are then investigated with numerical and analytical methods to characterize the dynamics of asymmetrically bistable modules. The assembly of such modules into greater structures generates complex, multi-well energy landscapes with stable system configurations exhibiting different quantities of stored elastic potential energy. Dynamic analyses illustrate the ability of these structures to capture a portion of the initial kinetic energy due to impulsive excitations as recoverable strain potential energy, and reveal how stiffness parameters, damping, and the presence of thermal noise in micro- and nano-scale applications influence energy capture behaviors. The insights gained could foster the development of advanced structural/material systems inspired by skeletal muscle, including actuators that effectively capture, store, and release energy, as well as adaptive, robust, and reusable armors and protective devices.

Keywords: multistable, energy capture, skeletal muscle, transient dynamics

(Some figures may appear in colour only in the online journal)

1. Introduction

The mechanics of skeletal muscle exhibit several noteworthy characteristics, including adaptability, robustness, and the ability to effectively store, convert, and release energy [1, 2], providing great inspiration for the development of advanced engineered structural/material systems. These macroscale properties of skeletal muscle are strongly influenced by the synergies among constituents across length scales, as presented in figure 1. Muscle fibers are composed of bundles of myofibrils, which in turn are held together by chains of actin and myosin proteins sectioned into units known as

[3] Author to whom any correspondence should be addressed.
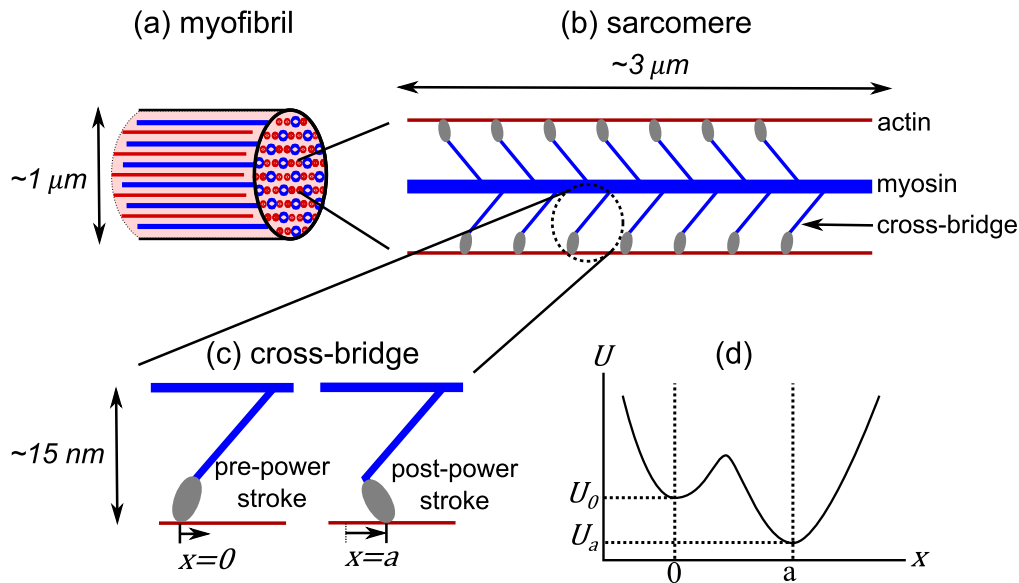
Figure 1. Schematic of skeletal muscle microstructure with approximate dimensions of constituents [3, 8]. Muscle fibers are composed of bundles of (a) myofibrils, which themselves consist of (b) chains of sarcomeres. The actin (thin) and myosin (thick) filaments that form the sarcomere's structure are connected by (c) cross-bridges extending from myosin. While the cross-bridge heads are bound to actin, they undergo a power stroke, generating forces which contribute to macroscopic muscle contractions [3]. (d) Mechanical models of cross-bridge power stroke motions incorporate elements with asymmetrically bistable potential energy landscape, reflecting a bias towards the post-power stroke state.

sarcomeres [3, 4]. When skeletal muscle is activated, cross-bridges extending from the myosin filament bind to sites on the actin filament and undergo power stroke motions, generating forces to enable sarcomere contractions. Models of power stroke mechanics often incorporate a bistable constituent whose two energy minima denote the pre- and post-power stroke configurations [5, 6]. The pre-power stroke state (also referred to as the *long* or *unfolded* configuration) has higher potential energy than the post-power stroke state (*short* or *folded* configuration), which means that the energy landscape of the bistable power stroke element is asymmetric. This is a result of differing chemical activity associated with adenosine triphosphate consumption that biases the power stroke towards the short configuration [7].

Recent research suggests that a significant proportion of the inertial energy from external inertial loads such as a periodically moved appendage is stored as strain energy in the cross-bridge constituent [9]. This stored energy may be later used to reduce the energetic cost of cyclic motion or to enable explosive movement [10, 11]. Certain external loads have also been shown to cause power stroke reversals, allowing the cross-bridge to move back and forth repeatedly along the power stroke's energy landscape without unbinding the myosin head from the actin binding site [12]. Models of these and other mechanics at the micro- and nano-scale commonly integrate constituents with non-convex energy landscapes to capture empirically-observed conformational changes [5, 13–16], and offer inspiration for the development of engineered structural/material systems that exhibit a similar ability to capture, store, and release energy. In fact, the exploitation of mechanical instabilities by incorporating bistable elements has been widely studied [17, 18], demonstrating significant damping [19, 20], energy dissipation
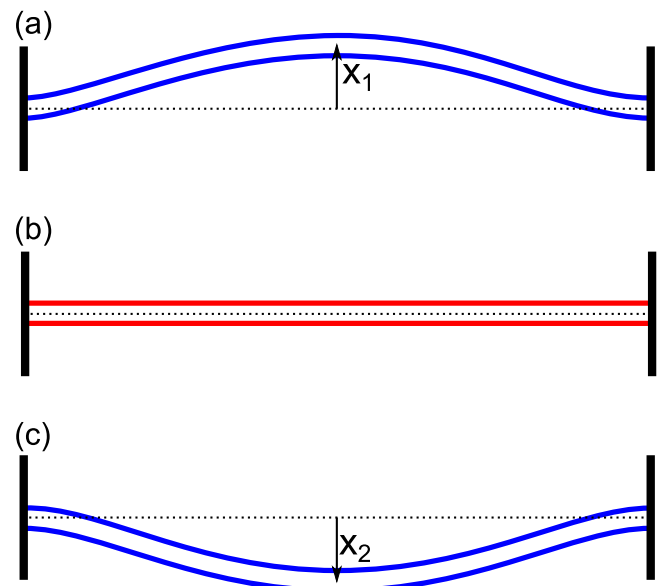
Figure 2. Axially compressed beam shown in three equilibrium configurations: (a) curved upward with vertical displacement of the beam midpoint $x = x_1$, (b) no vertical displacement or $x = 0$, and (c) curved downward with vertical displacement $x = x_2$. Configurations (a) and (c) are stable, while (b) is unstable.

[21–23], and shock absorption [24] as outcomes to the strategic exploitation. These behaviors arise primarily as a result of a phenomenon known as *snap-through* between stable equilibrium states of the structure's bistable constituents.
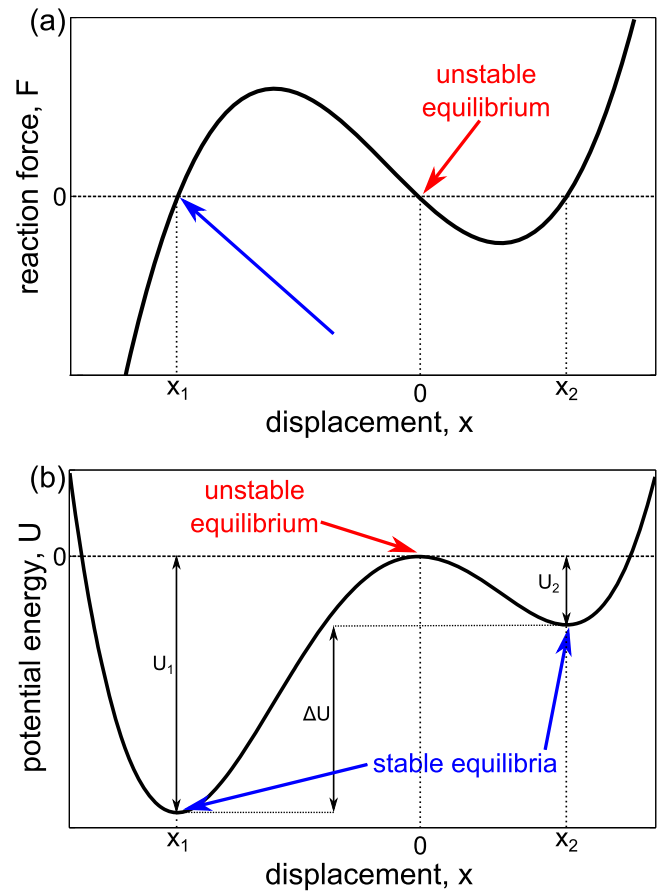
A common physical realization of a bistable element takes the form of a clamped, post-buckled beam as depicted in figure 2. The beam exhibits two stable configurations where the displacements of the beam's midpoints are $x = x_1$ and
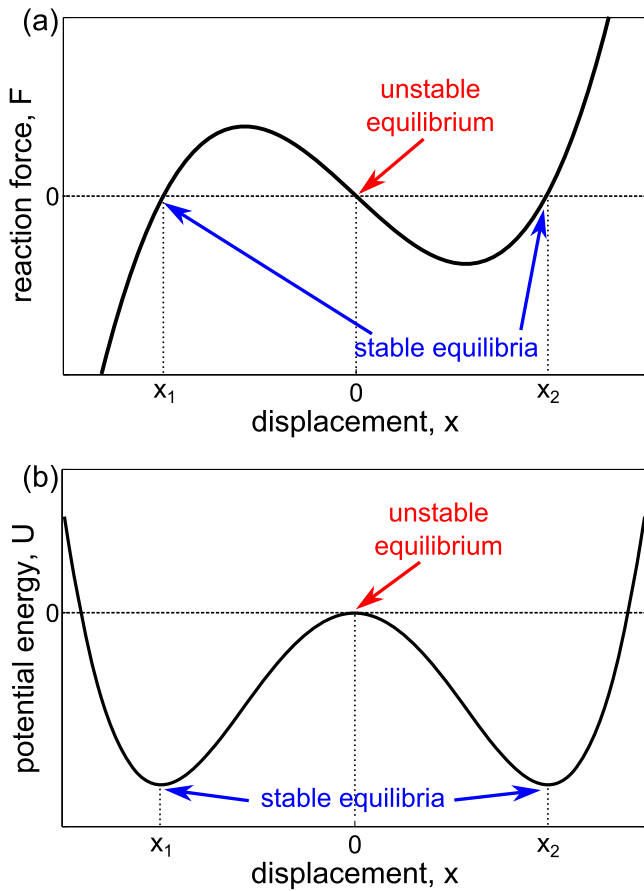
Figure 3. (a) Vertical reaction force at the beam midpoint in figure 2, and (b) potential strain energy as displacement x is varied of a symmetric bistable constrained curved beam. Equal amounts of strain energy are stored at the two stable equilibria.

Figure 4. (a) Vertical reaction force at the beam midpoint in figure 2, and (b) potential strain energy as displacement x is varied of an asymmetrically bistable constrained curved beam. Different amounts of strain energy are stored at the two stable equilibria. Transition from x_1 to x_2 requires a quantity of energy U_1 to be supplied to the system, and results in net strain energy storage of $\Delta U = U_1 - U_2$.

$x = x_2$, as shown in figures 2(a) and (c), respectively. An unstable equilibrium is observed at the neutral position for $x = 0$, as shown in figure 2(b). If the post-buckled beam is straight in its unstressed state, the reaction force as the beam midpoint is vertically displaced follows a curve similar to figure 3(a), with stable equilibria observed where the curve crosses the zero axis with positive stiffness or positive slope, and an unstable equilibrium where it crosses the zero axis with negative slope. The corresponding strain energy landscape is shown in figure 3(b), where the two local potential minima at the same energy level denote the two stable equilibria of this *symmetrically bistable* element. A beam with a natural curvature which is then clamped in its post-buckled state will be biased towards one of its two stable configurations [25], exhibiting *asymmetric bistability* and demonstrating reaction force and energy profiles represented by figure 4. The two local energy minima are at different levels, and a transition from the low-energy configuration $x = x_1$ to the high energy configuration $x = x_2$ results in the capture of recoverable strain energy of the amount $\Delta U = U_1 - U_2$.

There are several examples of structural/material systems that exhibit differences in elastic potential energy between stable equilibrium configurations under tensile [26, 27] and compressive [28, 29] loading. These architected structures and materials exhibit larger strains before failure

than the corresponding monolithic bulk material properties would permit, offering great potential for energy absorption and damage mitigation. While the energy trapping capabilities of such systems have been reported [26, 28], no connection has yet been made between the asymmetries inherent to the strain energy landscapes of these structures, though the mechanics described in figure 4 suggest that the asymmetric bistability inherent to these architectures may be the underlying reason for such intriguing properties. In the context of skeletal muscle, asymmetrically bistable elements are employed to explain not only the behaviors of individual cross-bridges and sarcomeres, but also those of the protein titin, which behaves as a shock or impact absorber in sarcomeres and may be represented mechanically as a series chain of bistable constituents [30]. Furthermore, though there have been efforts to understand the impact or shock isolation behaviors of structures incorporating bistable or negative-stiffness constituents [21, 24, 31], these investigations do not attempt to explain the strain energy capture that may result from the observed state transitions or snap-through events.

Based on the review and discussions above, the objectives of this research are to study the influence of asymmetry on the potential energy landscapes of structures composed of
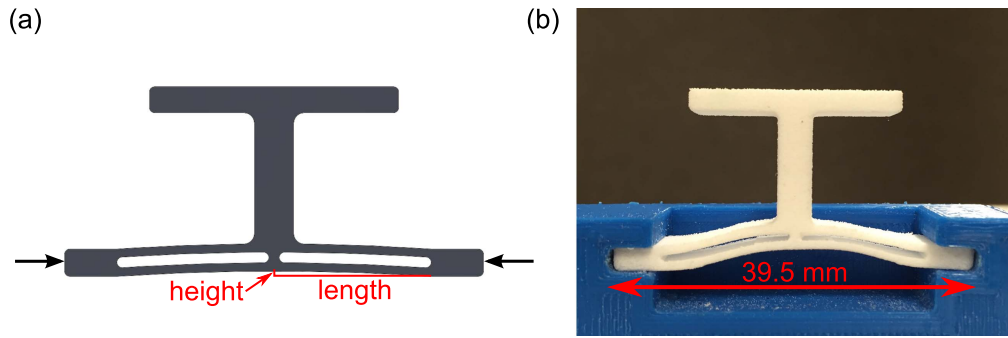
Figure 5. (a) Schematic of a single module composed of a connected, double curved arch with a stiff, T-shaped member to facilitate modular assembly. The unstressed beam curvature is calculated as height/length, and axial compression and constraint of double-curved beams enables bistability. (b) An experimental prototype fabricated with a beam length of 15 mm using selective laser sintering (SLS) of polyamide PA 2200 nylon is shown in its post-buckled, axially compressed position. The prototype's total initial width is 40 mm, but it is compressed and confined to a width of 39.5 mm by the rigid base.

bistable constituents, to exploit transitions between stable states to demonstrate strain energy capture under quasi-static and dynamic loads, and to understand the influences of structural parameters on system dynamics and energy capture. Insights into these behaviors would enable the development of structural/material systems that reflect skeletal muscle's robustness and its remarkable ability to store, convert, and release energy. In the following sections, experimental prototypes of single bistable elements with varying asymmetry are studied for their potential energy landscapes. A system identification is developed from experimentally-obtained force–displacement profiles, facilitating analytical and numerical investigations of the behavior of a single asymmetrically bistable element under dynamic loads. Energy landscapes of structures composed of multiple elements arranged in series are then studied, and dynamic analyses are conducted on their energy trapping capabilities. The influences of asymmetry, damping, excitation level, and thermal noise on energy trapping behaviors are analyzed and discussed, followed by concluding remarks.

2. Asymmetric force and energy landscapes in a bistable module

To facilitate investigations into the influence of asymmetry on the mechanics and energy landscapes of bistable elements, modules with varying geometries are designed and fabricated with polyamide PA 2200 nylon using selective laser sintering (SLS). A connected, double curved-beam design minimizes the likelihood that the element will buckle or snap-through in its second mode [24, 25], ensuring predictable and repeatable buckling behaviors. Figure 5(a) presents a schematic of a module in its unstressed state. The beam's curvature is defined as the ratio between the half-arch's height and its length, and its T-shaped member facilitates modular assembly. Figure 5(b) shows a prototype module in its post-buckled state under axial confinement of 39.5 mm in the lower-energy stable configuration. Quasi-static tests are performed using an Instron 5950 universal testing machine to obtain force–displacement relationships, and representative plots for three

modules of different unstressed beam curvatures are shown in figure 6. The modules with the greater unstressed curvature exhibit larger positive reaction forces under compression but smaller negative reaction force, meaning an increase in unstressed beam curvatures leads to greater asymmetry in the force–displacement profile. The most asymmetric module requires a relatively large compressive force to snap to the second stable configuration, while only needing a small tensile force in order to snap back to the initial state.

Experimentally-derived strain potential energy curves, shown by the solid lines in figure 7, are generated by integrating the reaction force curves with respect to displacement during the compressive portion of the quasi-static load tests. As the beam curvature is increased, the difference between the two local minima of strain energy grows larger and the energy landscape becomes increasingly asymmetric. To facilitate further numerical and analytical study of these asymmetrically bistable modules, it is assumed that the observed reaction force F_R of the modules may be approximated by a cubic nonlinearity, namely:

$$F_R = k_1 x + k_2 x^2 + k_3 x^3, \qquad (1)$$

where x represents the displacement of the midpoint of the double curved beams from the unstable equilibrium position, and k_1, k_2, and k_3 are the linear, quadratic, and cubic stiffness parameters, respectively. The potential strain energy U due to elastic deformation may be obtained by integrating the restoring force with respect to x.

$$U = \tfrac{1}{2}k_1 x^2 + \tfrac{1}{3}k_2 x^3 + \tfrac{1}{4}k_3 x^4 + C, \qquad (2)$$

where C is the integration constant. For consistency, U is prescribed to be zero at the unstable equilibrium $x = 0$, which corresponds to $C = 0$. The dashed curves in figure 7 depict the strain energies using equation (2) where the stiffness terms k_1, k_2, and k_3 are obtained from a polynomial fit to the experimental data, and the approximations reasonably reflect the strain energy curves of the evaluated modules. Furthermore, the quadratic stiffness k_2 demonstrates the greatest variation between modules of different beam curvature while k_1 and k_3 are relatively similar for all three tested samples, which suggests that variations in the asymmetry of the
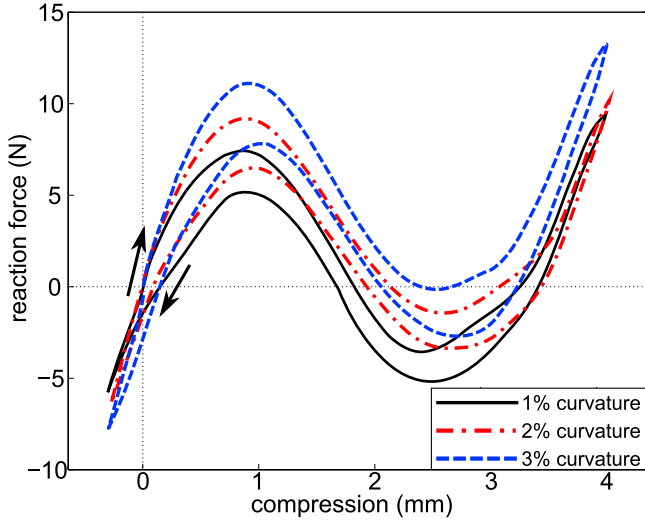
Figure 6. Force–displacement profiles of individual asymmetrically bistable modules obtained from uniaxial compression tests at a rate of 0.05 mm s^{-1}. As natural beam curvature is increased, the force–displacement characteristic grows more asymmetric with respect to the zero axis.
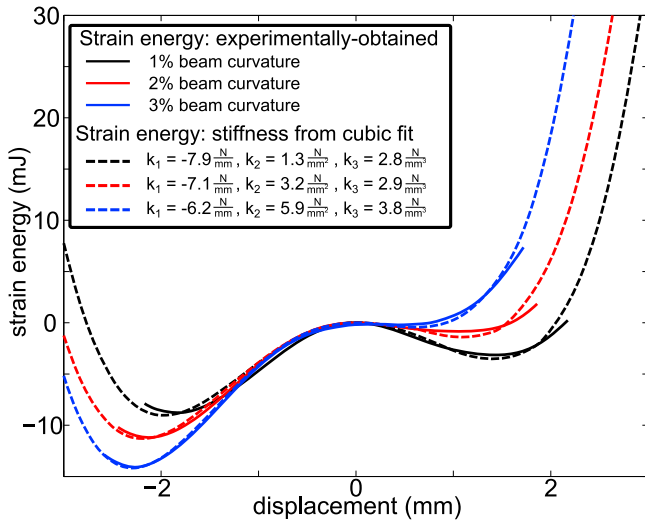
Figure 7. Strain energy profiles of three prototypes with varying unstressed beam curvature obtained from quasi-static compression tests (solid lines), demonstrating greater asymmetry of the double well potential energy landscape as beam curvature is increased. Dashed lines illustrate strain energy calculated from equation (2), where the nonlinear stiffness coefficients are obtained from a least-squares regression of cubic nonlinear stiffness parameters to experimental data.

module's strain energy landscapes could be modeled by tailoring k_2. This is confirmed by an examination of the strain energy expression in equation (2), where the quadratic stiffness k_2 contributes the only odd term and hence dictates the level of asymmetry. The cubic nonlinear stiffness approximation enables a systematic analytical and numerical dynamics study of the influence of various system and

excitation parameters on strain energy landscapes and energy trapping performance.

3. Force and energy landscape of a multi-module system

Mechanical models of skeletal muscle often incorporate serially-connected bistable elements in representations of sarcomere chains that form muscle myofibrils [15, 32], and the protein titin, which acts as a shock absorber in sarcomeres [30, 31]. Assembly of asymmetrically bistable elements into these greater structures leads to more complex force–displacement and strain energy landscapes, enabling large macroscopic length changes, shock absorption, and energy dissipation. This configuration may also be leveraged to demonstrate the capture and storage of elastic potential energy in the system's many stable configurations. For a structure composed of *n* serially connected bistable modules as depicted in figure 8, and whose reaction forces are governed by equation (1), the total strain energy stored in the system is:

$$U_{\text{tot}} = \frac{1}{2}k_{1,1}x_1{}^2 + \frac{1}{3}k_{2,1}x_1{}^3 + \frac{1}{4}k_{3,1}x_1{}^4$$
$$+ \sum_{j=2}^{n}\left(\frac{1}{2}k_{1,j}(x_j - x_{j-1})^2 + \frac{1}{3}k_{2,j}(x_j - x_{j-1})^3\right.$$
$$\left. + \frac{1}{4}k_{3,j}(x_j - x_{j-1})^4\right), \tag{3}$$

where x_j is the displacement and $k_{1,j}$, $k_{2,j}$, and $k_{3,j}$ are the linear, quadratic, and cubic stiffness coefficients, respectively, of the *j*th module.

To demonstrate the mechanics of systems composed of serially-configured modules, figures 9(a) and (b) present experimentally-obtained reaction force profiles of a structure composed of two and four modules, respectively, with 2% beam curvature. Positive slope or stiffness denotes the existence of stable configurations, and negative slopes correspond to regions of transition between stable states. The four-module structure demonstrates a greater number of stable configurations and much greater hysteresis over the compression and extension cycle. This is due to increased free-play in the structure and the increased likelihood of divergence between loading and unloading paths as the number of elements in a bistable chain is increased [13, 31]. For a single bistable element, the loading and unloading paths are theoretically identical, since there is only one stable configuration for a prescribed displacement. In a structure composed of $n = 2$ *identical* bistable elements with cubic nonlinearity, there may be multiple possible configurations for a range of global displacements, but they are at identical strain energy levels and thus do not demonstrate hysteresis [33]. Such a structure would exhibit smoothly varying strain energy under loading and unloading. However, for $n > 2$ or for $n = 2$ *different* modules, these coexistent configurations may be at different energy levels, and as the structure is globally extended or compressed, it does not follow the minimum-energy *Maxwell path* [13]. Instead, the large hysteresis observed in figure 9(b) is due to discrete state transitions that result in a decrease of
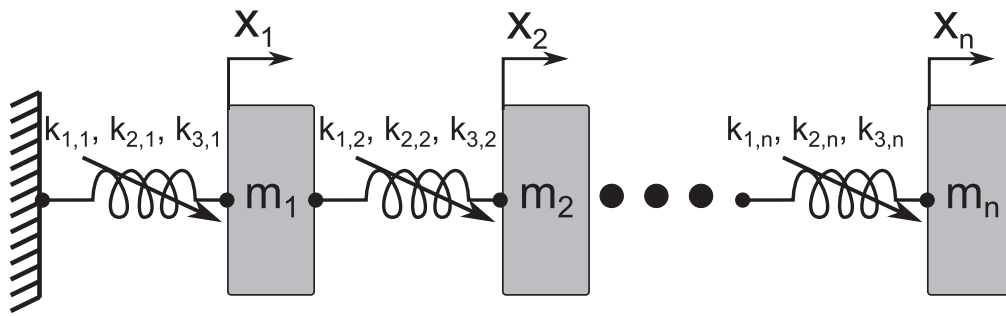
Figure 8. Schematic of a structure composed of *n* modules in series with bistability modeled using a cubic nonlinear stiffness.
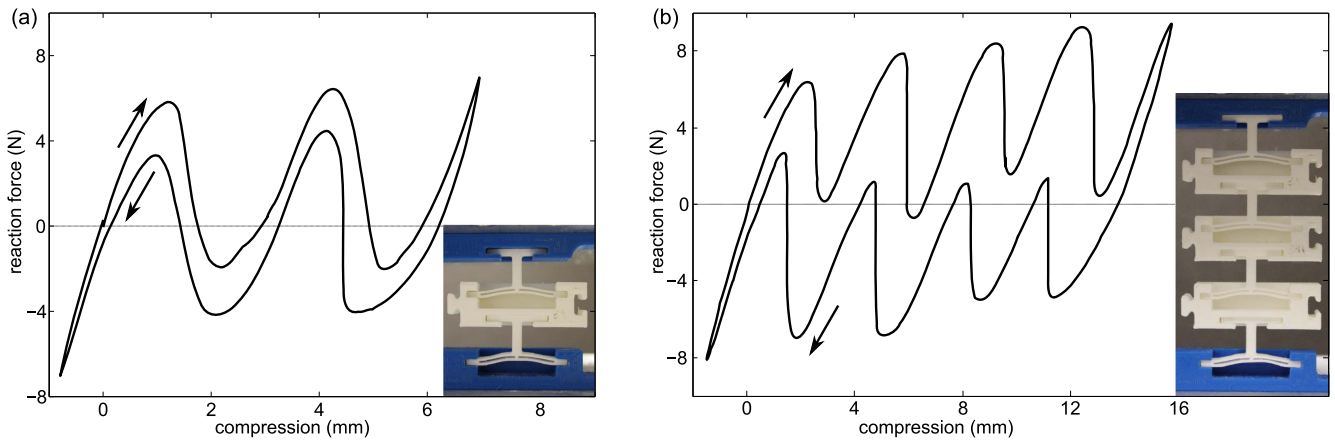
Figure 9. Observed reaction force of a (a) two-module structure and (b) four-module structure under uniaxial compression tests at a rate of 0.05 mm s^{-1}.
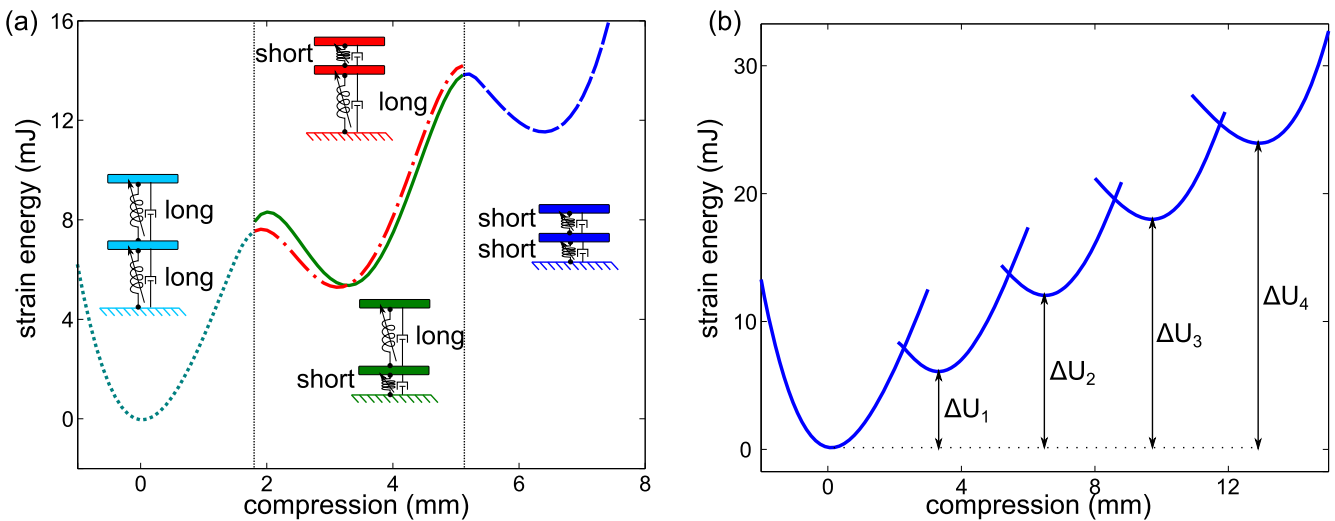
Figure 10. Strain energy landscape of a (a) two-module and (b) four-module structure calculated using a cubic stiffness approximation to experimentally-observed reaction force of a module with 2% beam curvature. A small difference between the stiffness terms of the two modules is provided in (a) in order to clearly illustrate the existence of multiple configurations. The four-module structure demonstrates overlapping potential wells, a feature found in chains of $n > 2$ bistable elements [31]. Due to the individual modules' asymmetry, increasing amounts of strain energy, ΔU_1 to ΔU_4, are stored at the stable equilibria—or local energy minima—as the structure is compressed.

potential energy when the structure's current configuration becomes unstable and the system snaps to a different stable configuration at a lower energy level, releasing stored elastic energy in the process [20, 31, 34].

Due to discrete state transitions that release elastic potential energy, direct integration of the experimentally-obtained force displacement profiles of structures composed of multiple elements does not in general yield their strain energy landscapes. To gain insight into the energy landscapes of two- and four-module structures, figure 10 presents the strain energy as computed from equation (3) where each module's nonlinear stiffness coefficients are obtained from

the system identification results shown in figure 7. For the two-module case in figure 10(a), random variation corresponding to a standard deviation of 5% from the nominal values is applied, accounting for manufacturing variability between the nominally identical modules and to facilitate clearer presentation of the ranges under which the different stable configurations may be observed. These configurations are denoted by different line styles and correspond to the presented figure insets. The assembly of multiple modules in series gives rise to a *metastability range* [35], where multiple reaction forces and strain energies may be observed for a range of end displacements x_2 due to the *coexistence* of multiple stable configurations, although only one configuration may be physically realized at a given time. If the modules were identical, the two global configurations in which one module in the short state and the other is in the long state would exhibit overlapping energy levels [33]. However, the modules are slightly different, and discontinuities are observed between the cyan dotted and green solid curves, and between the red dashed–dotted and blue dashed curves of figure 10(a). Under an external axial load, the structure will only exhibit state transitions that are continuous in potential energy or that result in a discrete reduction of stored strain energy [34, 36]. For the four-module case presented in figure 10(b), no random variation is applied to the modules' stiffness parameters and all modules are assumed to be identical. The local minima of potential energy, which denote the stable configurations in the absence of external forces, are at different quantities depending on the number of modules in the long (low-energy) and short (high-energy) configurations. Hence, a transition from the lowest energy global configuration to higher-energy configurations will result in incremental amounts of captured and stored elastic energy ΔU_1 to ΔU_4, depending on the number of long-to-short state transitions that occur.

4. Dynamics of an asymmetrically bistable oscillator

The quasi-static analysis in the prior section demonstrates that modular assembly of asymmetrically bistable constituents can lead to structures exhibiting complex, multi-well energy landscapes and whose stable configurations exhibit different quantities of stored elastic potential energy. Due to the modules' geometry, transitions from long to short configurations result in the capture and storage of recoverable strain energy. On the other hand, for structures under dynamic loads, the total system energies do not smoothly follow potential energy landscapes. Since the captured strain energy ΔU depends on the initial and final configurations of the system, transient dynamics play an important role in the structure's ability to capture energy in consequence to excitations. The experimental prototypes presented in the prior section, while not well-suited to dynamic tests at this stage of research due to their large damping, viscoelasticity, and low toughness, motivate comprehensive analytical and numerical investigations of these dynamics. Figure 11 presents a schematic of a one degree-of-freedom system based on the
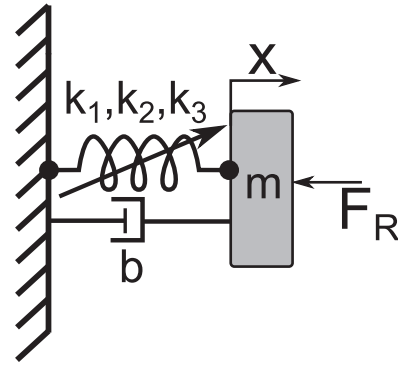
Figure 11. Schematic of a Duffing oscillator. k_1, k_2, and k_3 are the linear, quadratic and cubic stiffness coefficients of the nonlinear spring. The oscillator is bistable for $k_1 < 0$ and asymmetric for $k_2 \neq 0$.

experimentally-derived single-module mechanics shown in figures 6 and 7. The bistable nonlinear stiffness takes the cubic form of equation (1), while inertial influences are captured by the mass m, and linear viscous damping is assumed with coefficient b. The governing equation is thus:

$$m\ddot{x} + b\dot{x} + k_1 x + k_2 x^2 + k_3 x^3 = 0. \tag{4}$$

Equation (4) describes the dynamics of a Duffing oscillator [37], and under the specific conditions $k_1 < 0$, $k_2 \neq 0$, and $k_3 > 0$, it describes an asymmetric bistable Duffing oscillator. For the case of a single asymmetric Duffing oscillator starting in its lower-energy configuration, energy trapping due to an impulsive excitation may be quantified by comparing the difference in potential energy between its initial and final states with the initial kinetic energy of the impulsive excitation. Hence, if the initial and final configurations are identical, all of the initial kinetic energy is dissipated and no energy is trapped. If, however, the system settles in its higher-potential energy well, a portion of the initial kinetic energy is now captured.

Predicting the system's final configuration following impulsive excitation necessitates solving for its transient dynamics. Solution methods that assume the dynamics can be described using trigonometric functions lead to poor accuracy for large nonlinearities [38]. Jacobian elliptic functions have been proposed as generating solutions for the Duffing equation, with considerable success for undamped, bistable Duffing oscillators [37, 39]. Recently, Zhang *et al* [40] presented a solution method for the damped snap-through and intrawell vibrations of a symmetric bistable Duffing oscillator. However, this approach cannot be directly applied to the case of an asymmetric Duffing oscillator due to the assumed symmetric form of the Jacobian elliptic function $cn(u_c, k_c)$, so the method is adapted and modified. First, equation (4) is normalized by mass and rewritten as:

$$\ddot{x} + \eta\dot{x} + \alpha x + \beta x^2 + \gamma x^3 = 0, \tag{5}$$

where $\alpha = \frac{k_1}{m}$, $\beta = \frac{k_2}{m}$, $\gamma = \frac{k_3}{m}$, and $\eta = \frac{b}{m}$. In order to eliminate the quadratic stiffness β causing the asymmetry, the system is approximated by two different, symmetric bistable Duffing oscillators, each approximating the behavior of the
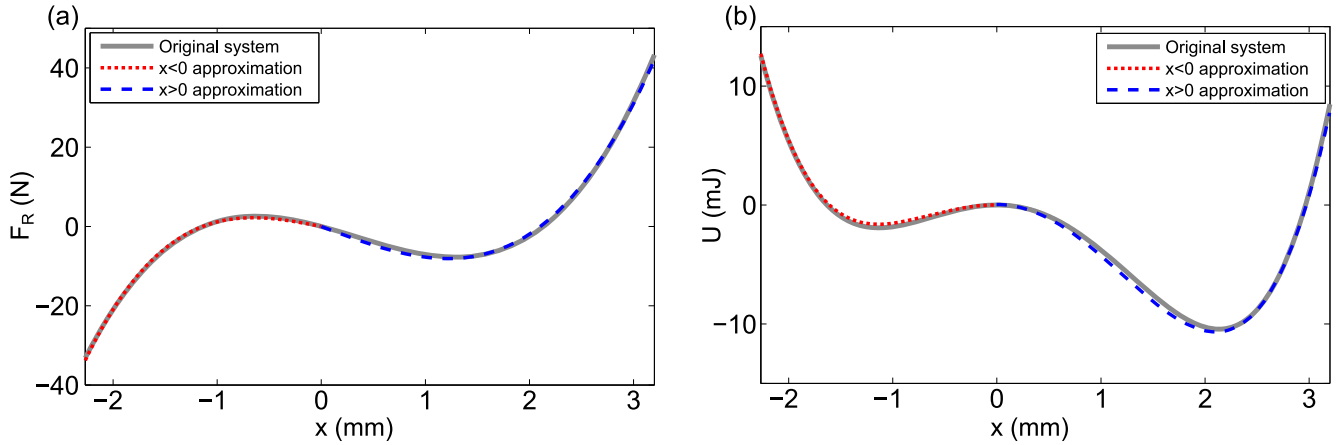
Figure 12. (a) Reaction force and (b) strain energy of an asymmetrically bistable Duffing oscillator. Solid curves denote the mechanics of the original asymmetric system described by equation (5), while the dotted and dashed curves denote the mechanics of the approximations of equations (6a) and (6b), respectively.

original system in one of the two potential wells.

$$\ddot{x} + \eta\dot{x} + \alpha_1 x + \gamma_1 x^3 = 0; \quad x \leqslant 0, \tag{6a}$$

$$\ddot{x} + \eta\dot{x} + \alpha_2 x + \gamma_2 x^3 = 0; \quad x > 0. \tag{6b}$$

The stiffnesses α_1, γ_1, α_2, and γ_2 are obtained from a least-squares regression of the asymmetrically bistable spring reaction force in equation (5). The validity of this approach for describing the force–displacement and potential energy profiles of the asymmetrically bistable spring is confirmed by figure 12 for $\alpha = -7.1$, $\beta = -3.2$, and $\gamma = 2.9$. The approximated stiffnesses are $\alpha_1 = -4.9$, $\gamma_1 = 4.0$ for $x < 0$, and $\alpha_2 = -10.4$, $\gamma_2 = 2.2$ for $x > 0$.

Given initial displacement and velocity x_0 and $\dot{x}_0$, the initial energy of the system is:

$$E_0 = \tfrac{1}{2}\dot{x}_0^2 + \tfrac{1}{2}\alpha_i x_0^2 + \tfrac{1}{4}\gamma_i x_0^4, \tag{7}$$

where $i = 1$ if $x \leqslant 0$ and $i = 2$ otherwise. If $E_0 > 0$, the initial oscillatory response is interwell, or snap-through, and is assumed to take the form:

$$x = C_1(t)cn(u_1, k_1); \quad x \leqslant 0, \tag{8a}$$

$$x = C_2(t)cn(u_2, k_2); \quad x > 0. \tag{8b}$$

$C_i(t)$ is the time-varying snap-through vibration amplitude, and u_i and k_i are the argument and modulus, respectively, of the cn Jacobian elliptic function. To compute initial amplitude and phase, the undamped case ($\eta = 0$) is first considered, hence the oscillation amplitude $C_i(t) = C_{i0}$ and modulus k_i are constants, and the argument u_i is:

$$u_i = \omega_i t + \phi_{i0}, \tag{9}$$

where ω_i is a constant parameter and ϕ_{i0} is the initial argument determined by initial conditions. Substituting equation (8) and its time derivatives into equation (6) yields the following:

$$\omega_i^2 = \gamma_i C_{i0}, \tag{10a}$$

$$k_i^2 = \frac{\gamma_i C_{i0}^2}{2(\gamma C_{i0} + \alpha)}. \tag{10b}$$

The Jacobian elliptic functions require k_i to be constrained such that $0 \leqslant k_i \leqslant 1$, which leads to the following condition:

$$0 \leqslant -\frac{\alpha_i}{\gamma_i C_{io}^2} \leqslant \frac{1}{2}. \tag{11}$$

Equations (6)–(10) are combined with the elliptic function identities $sn^2(u, k) + cn^2(u, k) = 1$ and $k^2 sn^2(u, k) + dn^2(u, k) = 1$ to yield the following expressions for initial amplitude, phase, and system energy:

$$C_{io} = \left(\frac{(-\alpha_i + ((\alpha_i + \gamma_i x_o^2)^2 + 2\gamma_i \dot{x}_0^2)^{\frac{1}{2}})}{\gamma_i} \right)^{\frac{1}{2}}, \tag{12a}$$

$$sn(\psi_{i0}, k_i)\frac{dn(\psi_{i0}, k_i)}{cn(\psi_{i0}, k_i)} = -\frac{\dot{x}_0}{\omega_i x_0}, \tag{12b}$$

$$E_0 = \tfrac{1}{4}C_{io}^2(2\alpha_i + \gamma_i C_{io}^2). \tag{12c}$$

Hence, $C_{io}^2 > -\frac{2\alpha_i}{\gamma_i}$ must be satisfied to ensure $E_0 > 0$, which is the condition under which snap-through oscillations are observed for the undamped case. If damping is present in the system, system energy will satisfy $E(t) \leqslant E_0$ for all $t \geqslant t_0$, so if the above condition on initial oscillation amplitude is not met, no snap-through events are predicted and oscillations remain confined to the local potential well. Following the solution approach for the damped, snap-through transient response of a symmetric bistable Duffing oscillator [40], where C_i, ω_i, u_i, and k_i vary with time, the following expression is obtained for the snap-through oscillation amplitude $C_i(t)$ and argument $u_i(t)$:

$$C_i(t) = \left[\left(\gamma_i^2 C_0^4 + \tfrac{a}{b}\alpha_i^2 \right)e^{-4b\eta_i t} - \tfrac{a}{b}\alpha_i^2 \right]^{\frac{1}{4}} \gamma_i^{-\frac{1}{2}}, \tag{13a}$$

$$u_i(t) = 4K_i\psi_i, \tag{13b}$$

where the coefficients $a = -0.785\,92$ and $b = 0.320\,51$ are parameters from a polynomial fit to permit an approximation of $\int \dot{C}_i(t)dt$ over an oscillation period, C_0 is the initial amplitude, and $K_i = K_i(k_i)$ is the complete elliptic integral of the first kind. By averaging over one period $4K_i$, the parameter ψ_i is approximated by:
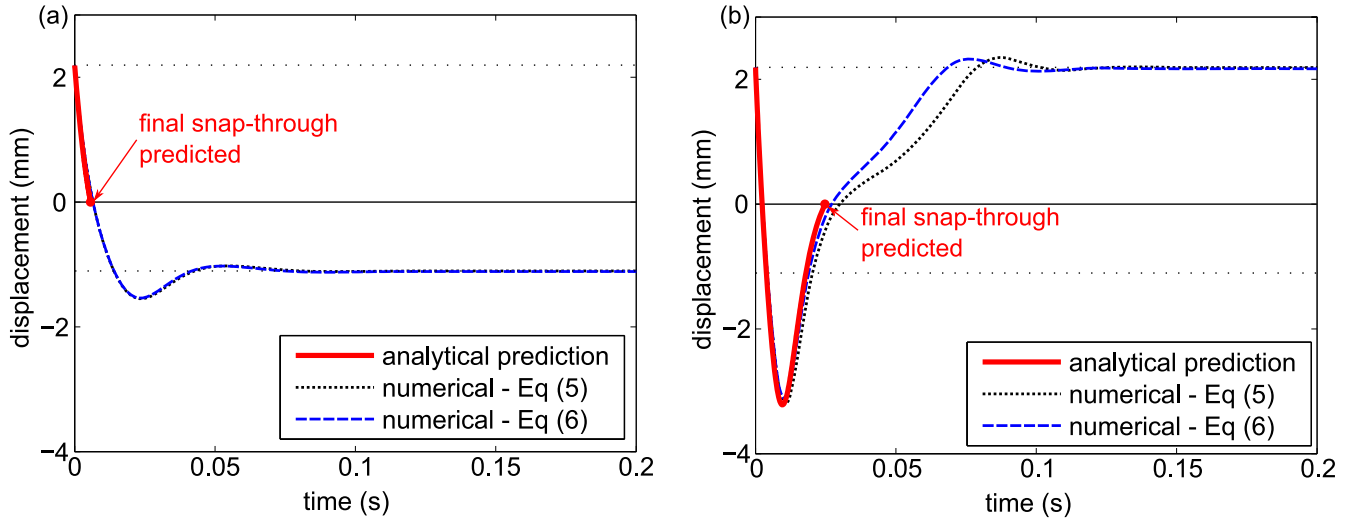
Figure 13. Analytically-predicted snap-through trajectories (solid), and numerically integrated trajectories using the asymmetric system of equation (5) and approximation of equation (6) in consequence to initial conditions (a) $x_0 = 2.2$ mm, $\dot{x}_0 = -0.45$ m s^{-1} and (b) $x_0 = 2.2$ mm, $\dot{x}_0 = -0.80$ m s^{-1}. In (a), the two numerically-integrated trajectories overlap almost completely. Thin, dotted horizontal lines denote the two stable equilibria. The analytical approach is demonstrated to accurately predict the final occurrence of snap-through, and hence the module's final configuration.

$$\psi_i(t) \cong \frac{\phi_{i0}}{4K_i} + \int_{t_0}^{t} \frac{\omega_i}{4K_i} dt \tag{14}$$

and the instantaneous displacement $x_i(t)$ may be computed according to equation (8). Recalling that the system will not undergo further snap-through oscillations for $C_i(t)^2 \leqslant -\frac{2\alpha_i}{\gamma_i}$, the time at which point snap-through oscillations are no longer predicted is found as:

$$t_{\text{end}} = -\ln\left[\frac{\left(4 + \frac{a}{b}\right)\alpha_i^2}{\left(\gamma_i^2 C_{i0}^4 + \frac{\alpha_i^2 a}{b}\right)}\right] \bigg/ 4b\eta_i. \tag{15}$$

The system switches between equations (8a) and (8b) each time a snap-through event occurs at $x(t_{\text{snap}}) = 0$. If $t_{\text{end}} > t_{\text{snap}}$, a new initial amplitude is found based on the parameters of the new local potential well as:

$$C_{j0} = \left[\frac{(-\alpha_j + (\alpha_j^2 + 2\gamma_j \dot{x}_{\text{snap}}^2))^{\frac{1}{2}}}{\gamma_j}\right]^{\frac{1}{2}}, \tag{16}$$

where $\dot{x}_{\text{snap}}$ is the velocity at time t_{snap}, and $j = 1$ for $\dot{x}_{\text{snap}} < 0$ and $j = 2$ for $\dot{x}_{\text{snap}} > 0$. Setting $t_0 = t_{\text{snap}}$, the procedure outlined in equations (13)–(16) is the repeated until $t_{\text{end}} < t_{\text{snap}}$, which is the condition that indicates that the final snap-through event has occurred and any further oscillations will remain confined to the local potential well as intrawell vibrations. Figure 13 illustrates the analytical procedure's accuracy in predicting the transient intrawell vibrations of a damped asymmetrically bistable Duffing oscillator under two different initial conditions: (a) $x_0 = 2.2$ mm, $\dot{x}_0 = -0.45$ m s^{-1} and (b) $x_0 = 2.2$ mm, $\dot{x}_0 = -0.80$ m s^{-1} The stiffness terms k_1, k_2, and k_3 are -7.1 N mm^{-1}, -3.2 N mm^{-2}, and 2.9 N mm^{-3}, respectively, which reflect the stiffness parameters obtained from the quasi-static tests presented in figure 6. Mass m and damping coefficient b are prescribed such that the linearized damping ratio and

undamped natural frequency at $x = x_0$ are $\zeta = 0.4$ and $\omega_n = 119$ rad s^{-1}, and are selected to reflect an underdamped oscillator capable of exhibiting the desired strain energy capturing behaviors under dynamic loads. The oscillator is initially at rest in its lower-energy stable configuration. Dotted lines show the trajectories as computed numerically using the original system description of equation (5), and dashed lines show the trajectory as computed numerically from the approximate systems of equations (6a) and (6b) in the two potential wells. Solid lines present analytically-predicted trajectories until the final snap-through event.

Under the initial conditions of the trajectories plotted in figure 13(a), the system is observed to undergo one snap-through event and settle in its higher-energy stable configuration, trapping a portion of the initial kinetic energy $T_0 = \frac{1}{2}m\dot{x}_0^2$ as recoverable strain energy. The fraction R of energy thus captured is computed as:

$$R = \frac{\Delta U}{T_0} = \frac{U_2 - U_1}{T_0}, \tag{17}$$

where U_1 and U_2 are the strain potential energy at the initial and final configurations, respectively. In figure 13(b) two snap-through events are observed, and the system settles in its low energy initial configuration resulting in no energy trapped ($R = 0$). The results of figure 13 demonstrate the ability of the presented analytical approach to predict the snap-through trajectories and final configuration of a damped asymmetrically bistable oscillator under impulsive excitation, and hence to predict the fraction of initial kinetic energy that is captured as recoverable strain energy.

5. Dynamics of a multi-module structure

The assembly of multiple elements in series greatly enhances opportunities for strain energy capture by leveraging state
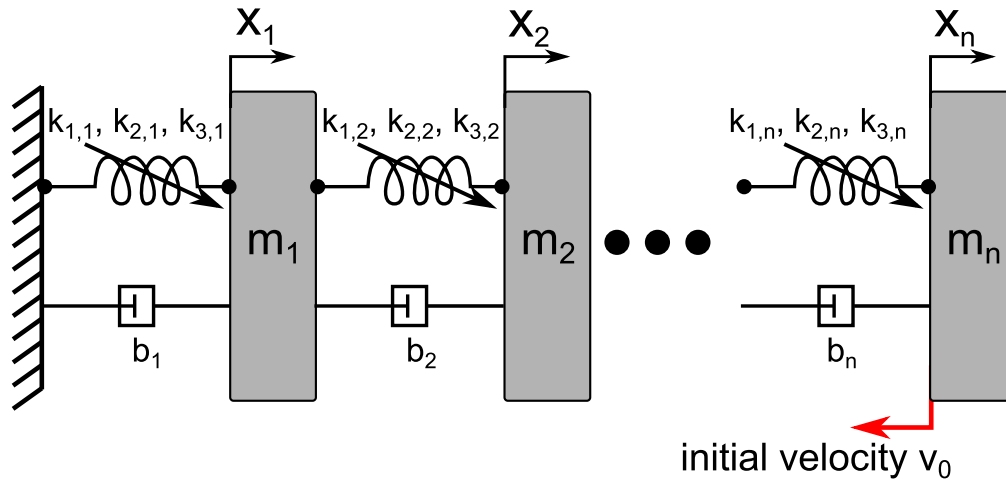
Figure 14. Schematic of a structure composed of *n* modules arranged in series. Initial velocity is prescribed to the end mass m_n in the indicated direction during dynamic analyses of energy trapping, simulating an impulsive excitation.

transitions between configurations at different energy levels. As illustrated in figure 10(b) for a structure composed of four serially connected modules, stable configurations exhibit increased stored energy as the structure is compressed and modules transition to the higher-energy short configurations. Assuming linear viscous damping and determining the reaction forces due to deflection in the cubic nonlinear springs connecting adjacent masses, the following equation of motion is obtained for mass m_j within a series configuration of *n* modules shown in figure 14.

$$m_j \ddot{x}_j + b_j(\dot{x}_j - \dot{x}_{j-1}) + b_{j+1}(\dot{x}_k - \dot{x}_{j+1}) + k_{1,j}(x_j - x_{j-1})$$
$$+ k_{1,j+1}(x_j - x_{j+1}) + k_{2,j}(x_j - x_{j-1})^2$$
$$+ k_{2,j+1}(x_j - x_{j+1})^2 + k_{3,j}(x_j - x_{j-1})^3$$
$$+ k_{3,j+1}(x_j - x_{j+1})^3 = 0. \tag{18}$$

The transient response is strongly influenced by the initial velocity and kinetic energy, as illustrated by the results presented in figure 15 for a four-module structure under different input energy levels. The stiffnesses $k_{1,j}$, $k_{2,j}$, and $k_{3,j}$ are -7.1 N mm^{-1}, -3.2 N mm^{-2}, and 2.9 N mm^{-3} for all modules. Each module has mass m_j and damping coefficient b selected such that the linearized natural frequency and damping ratio at each module's low-energy stable state are $\omega_{n_i} = 119$ rad s^{-1} and $\zeta_j = 0.4$, respectively. The initial velocity of the end mass is prescribed as v_0, and all other masses are stationary in the low energy state (long configuration). The thin, dotted horizontal lines indicate the five displacements x_4 of the end mass for stable configurations of the four-module structure. For an initial velocity $v_0 = 0.3$ m s^{-1}, shown by the solid line, the initial energy $T_0 = \frac{1}{2} m_4 v_0^2$ is insufficient to cause any of the four modules to snap through, and the structure remains in its initial configuration. For a slightly greater initial velocity of 0.5 m s^{-1}, shown by the thick dotted line, one of the structure's modules snaps through to its short configuration. Since $k_{2,j} < 0$ for all *j*, each module's short configuration has higher potential energy than its long state and a portion of the initial kinetic
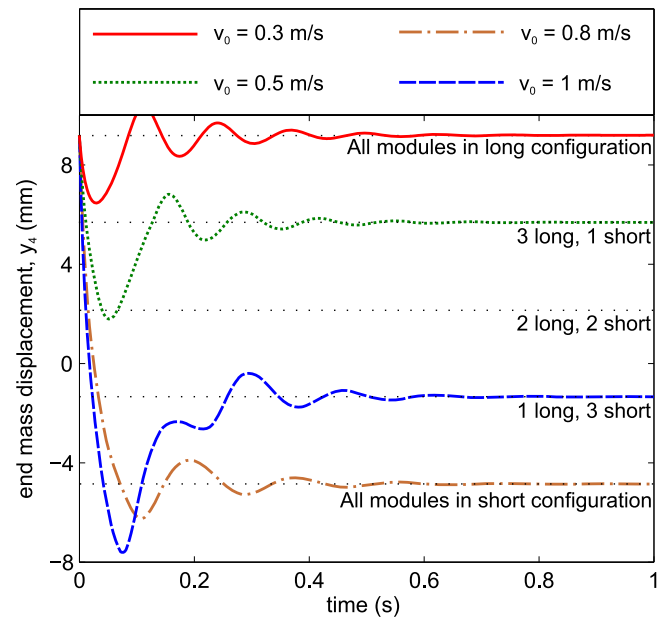
Figure 15. Displacements x_4 of a four-module structure's end mass due to impulsive excitations causing initial velocities v_0 when all modules are initially in their low-energy long configuraitons. Thin dotted lines indicate the five possible displacements under stable equilibrium conditions. The structure's final configuration is strongly dependent on excitation level.

energy is trapped as recoverable strain energy. An initial velocity $v_0 = 0.8$ m s^{-1}, indicated by the dash–dot line, causes all four modules to snap to the short state, maximizing trapped strain energy. However, if the initial velocity is increased to $v_0 = 1$ m s^{-1}, the residual kinetic energy after all modules have collapsed to their high-energy state is sufficient to force one module to escape its local potential well and snap back to the lower-energy long configuration, reducing the quantity of trapped strain energy.
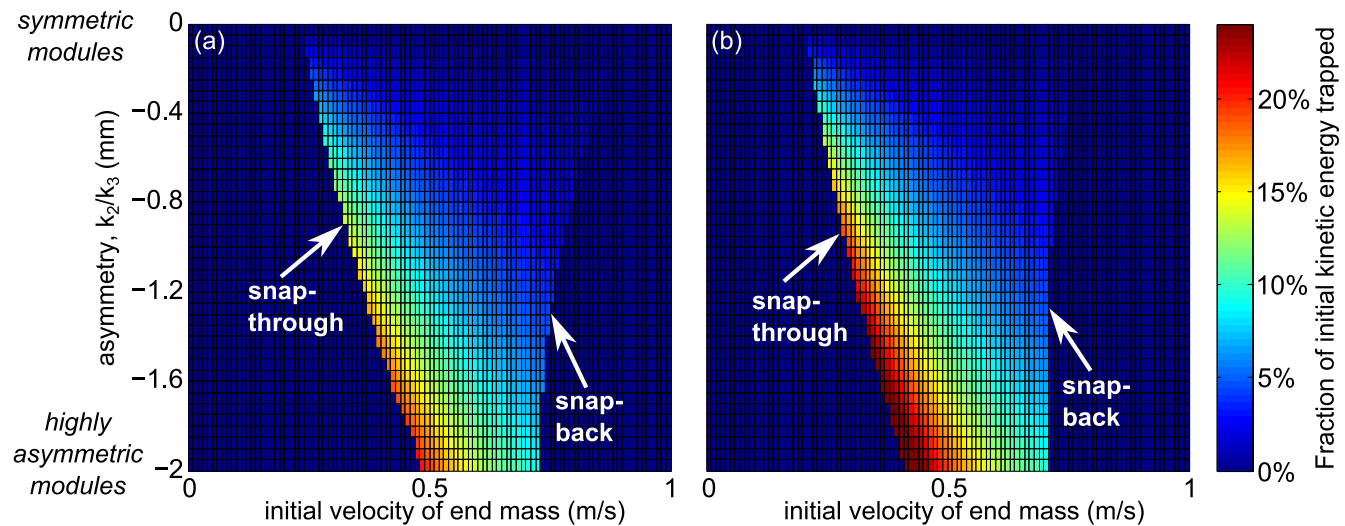
Figure 16. (a) Analytical prediction and (b) numerical simulation of fraction of initial kinetic energy T_0 from an impulsive excitation trapped as recoverable strain energy as level of asymmetry is varied under a range of initial velocities. Linear and cubic stiffness terms k_1 and k_3 are obtained from the cubic nonlinear approximation to the experimentally-obtained force–displacement profile shown in figure 6 of the module with 2% beam curvature. The quadratic stiffness k_2 is varied along the vertical axis to tailor the asymmetry. Boundaries demarcating the onset of snap-through and snap-back are clearly visible.

6. Energy capture under impulsive excitation

The four initial conditions for which trajectories are plotted in figure 15 result in four different final configurations and, due to the modules' asymmetric bistability, four different quantities of captured elastic potential energy ΔU. Energy trapping performance may be quantified using the ratio $R = \frac{\Delta U}{T_0}$, and by conservation of energy the total energy dissipated is $(1 - R)T_0$. While figure 15 demonstrates that input energy strongly influences the structure's final configuration, a systematic investigation is required in order to uncover the effects of varying structural parameters and excitation levels on energy trapping performance.

6.1. Strain energy capture in a single asymmetrically bistable module
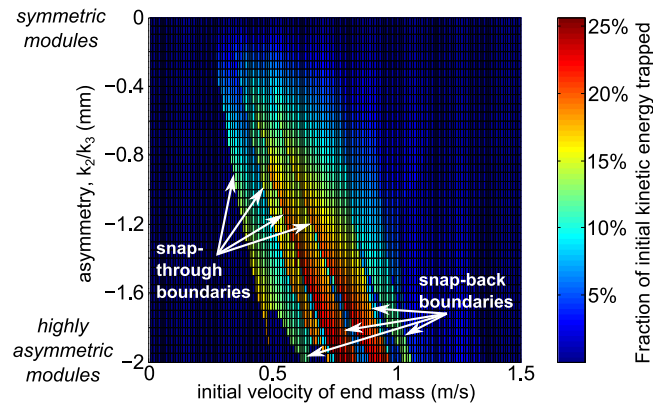
To illustrate these effects, figure 16 presents contour plots showing the fraction of initial kinetic energy that is captured as recoverable strain energy in a single asymmetrically bistable module under a range of initial velocities v_0 and different levels of asymmetry. The linear and cubic stiffness parameters employed in simulation and analysis are $k_1 = -7.1\ \mathrm{N\ mm^{-1}}$ and $k_3 = 2.9\ \mathrm{N\ mm^{-3}}$. Recalling that the asymmetry of a cubic nonlinear spring varies with k_2, the ratio $\frac{k_2}{k_3}$ is used as a measure of asymmetry. The module is initially at rest in its low-energy long configuration and prescribed a range of initial velocities v_0 in the direction of the unstable equilibrium. Dissipative effects are modeled with a linear damping coefficient selected such that the linearized damping ratio at the two stable equilibria of a symmetric module (where $k_2 = 0$) is $\zeta = 0.4$. Figure 16(a) presents analytically-predicted energy trapping performance using the approximation of equation (6) while figure 16(b) shows results from direct numerical integration of equation (5).

No energy trapping is observed for low initial velocities since the initial energy is insufficient to induce snap-through. The modules' initial and final configurations are hence identical. A clear boundary is apparent where the initial velocity, and consequently the initial kinetic energy, becomes sufficient to cause the module to snap-through and settle in the higher-energy state following trajectories qualitatively similar to figure 13(a). Very large initial velocities result in trajectories resembling figure 13(b), demonstrating no energy trapping due to the module snapping back to its low-energy configuration. The analytical prediction of these boundaries differs slightly from the numerically-obtained results, which is reasonable given that the analytical method employs an approximation of the original system. As asymmetry is increased, a greater initial velocity is required before snap-through and energy trapping are observed. The greatest fraction of trapped energy is observed for large asymmetry, which is consistent with the explanations of figures 3 and 4, because greater asymmetry increases U_1 while decreasing U_2, resulting in a larger potential energy difference ΔU. However, large asymmetries also show a smaller range of velocities for which energy trapping is observed before the module snaps back to its low energy configuration, resulting in no strain energy capture.

6.2. Strain energy capture in a four-module structure

While figure 10 demonstrates that a structure with asymmetrically bistable constituents will exhibit different quantities of stored energy in its stable configurations, its transient response and final configuration in consequence to dynamics loads depends strongly on input energy. To further understand these influences, figure 17 presents a contour plot showing the percentage of initial kinetic energy trapped as recoverable strain energy in a four-module structure under a range of

Figure 17. Fraction of initial kinetic energy T_0 that is trapped as recoverable elastic potential energy by the structure as the level of asymmetry and initial velocity of the end mass are varied. Linear and cubic stiffness parameters are obtained from a least-squares fit of a cubic nonlinear stiffness to the experimentally-obtained force–displacement profile of a module with 2% beam curvature. Damping coefficients are selected such that each module's linearized damping ratio is $\zeta = 0.4$ at the low-energy configuration. The discrete boundaries of energy trapping performance indicate the occurrence of snap-through and snap-back. Greatest energy trapping performance is observed at high asymmetry levels, but this comes with an increased risk of snap-back.

initial velocities v_0 and levels of asymmetry $\frac{k_2}{k_3}$, obtained via numerical integration of equation (18) using a fourth-order Runge–Kutta solver. Linear and cubic stiffness are nominally prescribed as $k_1 = -7.1$ N mm^{-1}. and $k_3 = 2.9$ N mm^{-3}, respectively, with a linearized damping ratio of $\zeta = 0.4$, but a random variation is applied to each module's parameters with a standard deviation of 5% of the nominal value. As the initial velocity v_0 is increased from 0, a clear color boundary is noted where the initial kinetic energy $T_0 = \frac{1}{2}mv_0^2$ is sufficiently lae to cause one of the four modules to snap through to the higher-energy short configuration. Four such boundaries are visible, corresponding to each of the four layers collapsing from the long configuration to the short configuration. Consistent with the single module case shown in figure 16, increasing the level of asymmetry results in a greater minimum initial velocity being required before energy trapping is observed. In addition, highly asymmetric modules have a large difference ΔU between stable configurations, enabling a greater portion of the initial kinetic energy to be captured as recoverable strain potential energy rather than lost due to dissipation.

The snap-back phenomenon is apparent in figure 17 where a sudden drop in energy trapping is observed as the initial velocity is increased, and explains the absence of energy trapping at very large initial velocities where all modules have snapped back to the long, low energy configuration. Snap-back boundaries are most pronounced for highly asymmetric modules where the energy difference between stable configurations is large, and these highly asymmetric structures exhibit only a small range of initial velocities for which peak energy trapping is observed. These results reveal that, when designing the level of asymmetry in energy trapping structures, a balance must be considered

between achieving the peak energy trapping required and minimizing the likelihood of snap-back.

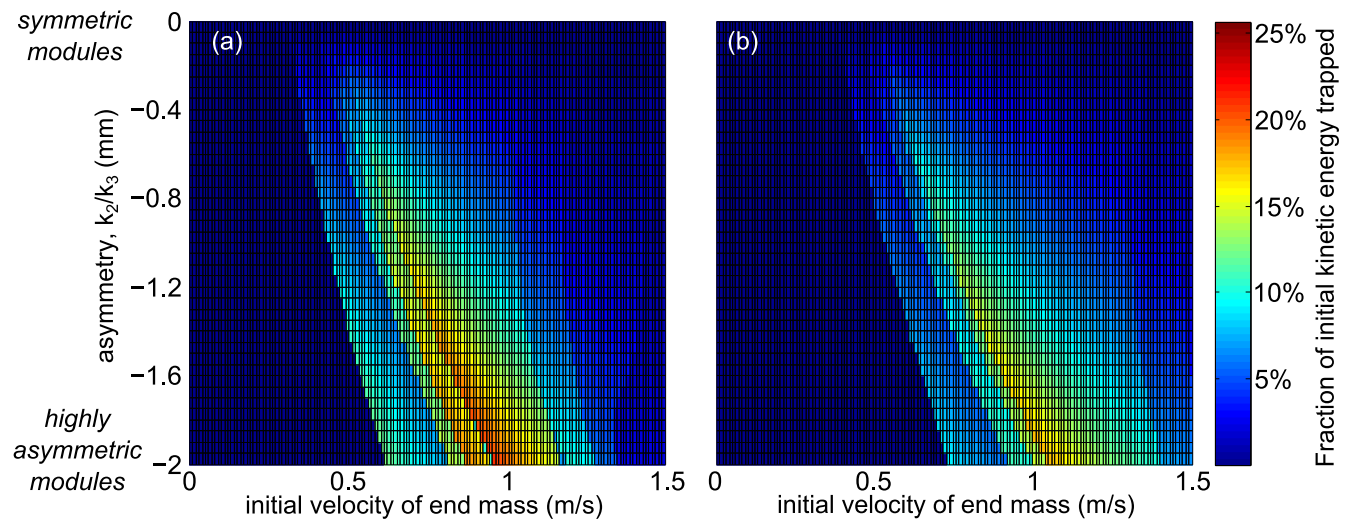### 6.3. Influence of viscous damping on energy capture

A structure's damping properties strongly influence energy trapping performance, since the conservation of energy requires that any portion of the initial kinetic energy T_0 that is not captured as strain energy must be dissipated. Hence, the fraction of initial kinetic captured as recoverable strain energy is $R = \Delta U/T_0$, while the ratio of captured to dissipated energy is $R/(1 - R)$. Figures 18(a) and (b) present contour plots with the same ranges of excitation level and asymmetry, and the same color scale as shown in figure 17. However, damping coefficients selected such that the modules' linearized damping ratios are now (a) $\zeta = 0.6$ and (b) $\zeta = 0.8$, respectively. Comparing the results of figure 18 with those in figure 17, it is observed that increased viscous damping reduces peak energy trapping performance by dissipating a greater proportion of the initial kinetic energy. Large amplitude snap-through events dissipate large quantities of energy, and this characteristic is enhanced as damping levels are increased, reducing the likelihood of further snap-through or snap-back events. Moreover, as damping is increased, greater initial velocities and kinetic energies are required to induce snap-through events.

Hence, large dissipation is undesirable from an energy trapping perspective since the objective is to capture, rather than dissipate, the initial kinetic energy as recoverable strain energy. However, large dissipation also reduces the likelihood of snap-back as the excitation level is increased. A balance is again observed between maximizing the fraction of initial kinetic energy that is trapped as recoverable strain energy, and maintaining robustness by minimizing the risk of snap-back to configurations at low strain energy levels.
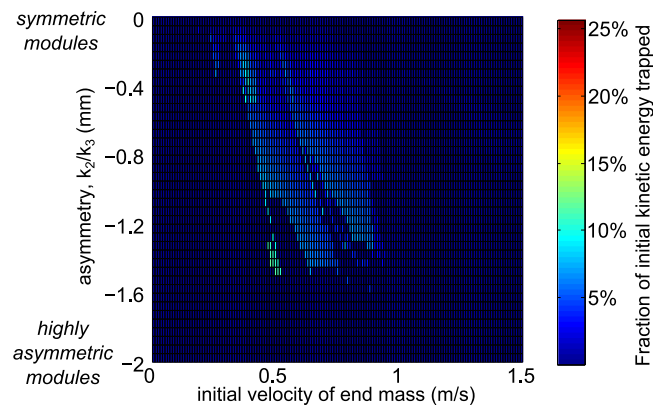
6.4. Influence of noise on energy capture

Thermal noise strongly influences the mechanics of muscle sarcomeres and cross-bridges. In fact, macroscopic length change and force generation is due to the combination of a control signal broadcast by the central nervous system and stochastic behaviors at the sarcomere level [41]. Local thermal noise acts as an additive white noise component to a nerve impulse, and collective behaviors arise due to the fact that a single motor neuron controls approximately a billion individual sarcomeres [3]. The nerve impulse influences the probability of sarcomere state transitions, and feedback from muscle spindles leads to the modulation of the control signal in order to enable fine, continuous macroscopic length change and force generation. However, thermal noise can also inhibit the energy storage, since elements may be more likely to escape shallow potential wells at high energy levels into lower-energy configurations. To understand these influences, and to guide the development of energy trapping devices for applications such as actuators and energy absorbing devices used on micro and nano length scales, simulations are performed using the stochastic differential equation (SDE)

Figure 18. Fraction of initial kinetic energy T_0 that is trapped as recoverable elastic potential energy by the structure, as the level of asymmetry and initial velocity of the end mass are varied when damping coefficients are selected such that the linearized damping ratios are (a) $\zeta = 0.6$ and (b) $\zeta = 0.8$ in the low-energy configurations. Compared with the results for $\zeta = 0.4$ in figure 17, larger damping ratios generally degrade energy trapping performance, but result in a reduced risk of snap-back at higher asymmetry levels. The portion of initial kinetic energy that is not captured must be dissipated, so the compromised energy trapping performance at higher levels of damping corresponds to a greater proportion of dissipated energy.

Figure 19. Energy trapping performance of a four-module structure for different levels of asymmetry and under various initial velocities v_0. The system's modules are also subject to white noise excitation with $\sigma = 3$ mm s^{-2}. The presence of noise compromises energy trapping at large levels of asymmetry.

Toolbox [42]. A four-module structure initially at the lowest-energy stable configuration with varying levels of asymmetry and a range of prescribed initial velocities, is subject to thermal noise modeled as a zero-mean random excitation on each module with a standard deviation $\sigma = 3$ mm s^{-2}. The susceptibility of bistable systems to snap-through may be strongly influenced by the presence of random excitations [43, 44], and given the modules' parameters developed in section 2, this level of noise is sufficient to prevent highly asymmetric modules from settling in their high energy states, and is employed to illustrate the corresponding effect on energy capture and storage. Figure 19 presents the resulting contour plot for simulations where nominal stiffness parameters of each module are those obtained from experimental force–displacement results of a module with 2% beam curvature. Compared with the results of figure 17, the addition of

noise is confirmed to greatly inhibit energy capture, with highly asymmetric structures exhibiting no energy trapping. Stochastic excitations are known to induce snap-through oscillations in Duffing-type bistable oscillators [45–47], and due to the relative depth of the potential wells of an asymmetrically bistable element and the energy required to overcome the local energy barrier, the presence of noise is more likely to cause transitions from the high-energy configuration to the low-energy configuration than vice versa. As a result, a structure comprised of highly asymmetric modules is less likely to trap and store energy in high-energy states without the occurrence of noise-induced snap-back. Thus, when designing strain energy capture devices in applications where stochastic influences are non-negligible, the degree of asymmetry should be strategically selected based on the expected magnitude of the noise.

7. Conclusions

The energetic versatility and functionality exhibited by skeletal muscle provides great inspiration for the development of advanced structures and materials. Inspired by these characteristics, and by the mechanics of muscle micro- and nano-scale building blocks—sarcomeres and cross-bridges—this research investigates the ability of modular structures composed of asymmetrically bistable constituents to capture and store recoverable strain energy in higher-energy stable configurations. Individual one-dimensional modules are designed, fabricated, and comprehensively studied, providing insight into how geometric parameters influence asymmetrically bistable strain energy landscapes. System identification enables analytical prediction of the transient dynamics of asymmetrically bistable modules using Jacobi elliptic

functions. Modular assembly of asymmetrically bistable constituents is then explored, generating complex, multiwall strain energy landscapes and enhancing opportunities for strain energy capture by exploiting the different energy levels of the structure's stable configurations. Lastly, the energy trapping behaviors of single modules and multiple-module structures under impulsive excitations is investigated, demonstrating their ability to capture a portion of the initial kinetic energy of the excitation as recoverable strain energy. The influences of asymmetry, dissipation, and noise are explored, revealing a balance between maximizing the amount of captured energy and minimizing the risk of the structure snapping back to its low-energy state. Ongoing efforts are underway to understand how the trapped energy may be effectively and efficiently released to enable useful mechanical work.

Acknowledgments

References

[1] Lombardi V, Piazzesi G and Linari M 1992 Rapid regeneration of the actin-myosin power stroke in contracting muscle *Nature* **355** 638–41

[2] Shimamoto Y, Suzuki M, Mikhailenko S V, Yasuda K and Ishiwata S 2009 Inter-sarcomere coordination in muscle revealed through individual sarcomere response to quick stretch *Proc. Natl Acad. Sci. USA* **109** 11954–9

[3] Lieber R L 2009 *Skeletal Muscle Structure, Function, and Plasticity* (Philadelphia, PA: LWW)

[4] Huxley A F and Simmons R M 1971 Proposed mechanism of force generation in striated muscle *Nature* **233** 533–8

[5] Caruel M, Allain J M and Truskinovsky L 2013 Muscle as a metamaterial operating near a critical point *Phys. Rev. Lett.* **110** 248103

[6] Marcucci L and Truskinovsky L 2010 Muscle contraction: a mechanical perspective *Eur. Phys. J.* E **32** 411–8

[7] Marcucci L and Truskinovsky L 2010 Mechanics of the power stroke in myosin II *Phys. Rev.* E **81** 051915

[8] Fuchs F and Wang Y P 1996 Sarcomere length versus interfilament spacing as determinants of cardiac myofilament Ca^{2+} sensitivity and Ca^{2+} binding *J. Mol. Cell. Cardiol.* **28** 1375–83

[9] Williams C D, Regnier M and Daniel T L 2012 Elastic energy storage and radial forces in the myofilament lattice depend on sarcomere length *PLoS Comput. Biol.* **8** e1002770

[10] Lappin A C, Monroy J A, Pilarski J Q, Zepnewski E D, Pierotti D J and Nishikawa K C 2006 Storage and recovery of elastic potential energy powers ballistic prey capture in toads *J. Exp. Biol.* **209** 2535–53

[11] Zack T I, Claverie T and Patek S N 2009 Elastic energy storage in the mantis shrimp's fast predatory strike *J. Exp. Biol.* **212** 4002–9

[12] Sellers J R and Veigel C 2010 Direct observation of the myosin-Va power stroke and its reversal *Nat. Struct. Mol. Biol.* **17** 590–5

[13] Benichou I and Givli S 2013 Structures undergoing discrete phase transformation *J. Mech. Phys. Solids* **61** 94–113

[14] Novak I and Truskinovsky L 2014 Nonaffine response of skeletal muscles on the 'descending limb' *Math. Mech. Solids* **20** 697–720

[15] Denoth J, Stussi E, Csucs G and Danuser G 2002 Single muscle fiber contraction is dictated by inter-sarcomere dynamics *J. Theor. Biol.* **216** 101–22

[16] Caruel M, Allain J M and Truskinovsky L 2015 Mechanics of collective unfolding *J. Mech. Phys. Solids* **76** 237–59

[17] Hu N and Burgeño R 2015 Buckling-induced smart applications: recent advances and trends *Smart Mater. Struct.* **24** 063001

[18] Harne R L and Wang K W 2017 *Harnessing Bistable Structural Dynamics: For Vibration Control, Energy Harvesting, and Sensing* (Chichester: Wiley)

[19] Johnson D R, Thota M, Semperlotti F and Wang K W 2013 On achieving high and adaptable damping via a bistable oscillator *Smart Mater. Struct.* **22** 115027

[20] Lakes R S 2001 Extreme damping in compliant composites with a negative-stiffness phase *Phil. Mag. Lett.* **81** 95–100

[21] Barbarino S, Pontecorvo M E and Gandhi F S 2012 Energy dissipation of a bi-stable von-mises truss under harmonic excitation *Proc. 54th AIAA/ASME/ASCE/AHS/ASC Structures, Structural Dynamics, and Materials Conf. (Honolulu, Hawaii, USA)* AIAA 2012–1712 (https://doi.org/10.2514/6.2012-3267)

[22] Kidambi N, Harne R L and Wang K W 2016 Adaptation of energy dissipation in a mechanical metastable module excited near resonance *J. Vib. Acoust.* **138** 011001

[23] Harne R L, Song Y and Dai Q 2017 Trapping and attenuating broadband vibroacoustic energy with hyperdamping metamaterials *Extreme Mech. Lett.* **12** 41–7

[24] Correa D M, Klatt T, Cortes S, Haberman M R, Desiderio K and Seepersad C C 2015 Negative stiffness honeycombs for recoverable shock isolation *Rapid Prototyping J.* **21** 193–200

[25] Qiu J, Lang J H and Slocum A H 2004 A curved-beam bistable mechanism *J. Microelectromech. Syst.* **13** 137–46

[26] Winkelmann C, Kim S S and La Saponara V 2010 Design and development of hybrid composite bistable structures for energy absorption under quasi-static tensile loading *Compos. Struct.* **93** 171–8

[27] Rafsanjani A, Akbarzadeh A and Pasini D 2015 Snapping mechanical metamaterials under tension *Adv. Mater.* **27** 5931–5

[28] Shan S *et al* 2015 Multistable architected materials for trapping elastic strain energy *Adv. Mater.* **27** 4296–301

[29] Restrepo D, Mankame N D and Zavattieri P D 2015 Phase transforming cellular materials *Extreme Mech. Lett.* **4** 52–60

[30] Benichou I and Givli S 2011 The hidden ingenuity of titin structure *Appl. Phys. Lett.* **98** 091904

[31] Cohen T and Givli S 2014 Dynamics of a discrete chain of bi-stable elements: a biomimetic shock absorbing mechanism *J. Mech. Phys. Solids* **64** 426–39

[32] Givli S and Bhattacharya K 2009 A coarse-grained model of the myofibril: overall dynamics and the evolution of sarcomere non-uniformities *J. Mech. Phys. Solids* **57** 221–43

[33] Puglisi G and Truskinovsky L 2000 Mechanics of a discrete chain with bi-stable elements *J. Mech. Phys. Solids* **48** 1–27

[34] Puglisi G and Truskinovsky L 2005 Thermodynamics of rate-independent plasticity *J. Mech. Phys. Solids* **53** 655–79

[35] Harne R L, Wu Z and Wang K W 2016 Designing and harnessing the metastable states of a modular metastructure for programmable mechanical properties adaptation *J. Mech. Des.* **138** 021402

[36] Oh Y S and Kota S 2009 Synthesis of multistable equilibrium compliant mechanisms using combinations of bistable mechanisms *J. Mech. Des.* **131** 021002

[37] Kovacic I and Brennan M J 2011 *The Duffing Equation: Nonlinear Oscillators and their Behaviour* (New York: Wiley)

[38] Yuste S B and Bejarano J D 1990 Improvement of a Krylov-bogoliubov method that uses jacobi elliptic functions *J. Sound Vib.* **139** 151–63

[39] Okabe T, Kondou T and Ohnishi J 2011 Elliptic averaging methods using the sum of Jacobian elliptic delta and zeta functions as the generating solution *Int. J. Non-Linear Mech.* **46** 159–69

[40] Zhang C, Harne R L, Li B and Wang K W 2016 Reconstructing the transient, dissipative dynamics of a bistable duffing oscillator with an enhanced averaging method and jacobian elliptic functions *Int. J. Non-Linear Mech.* **79** 26–37

[41] Ueda J, Odhner L and Asada H 2007 Broadcast feedback of stochastic cellular actuators inspired by biological muscle control *Int. J. Robot. Res.* **26** 1251–65

[42] Picchini U 2007 SDE Toolbox: simulation and estimation of stochastic differential equations with MATLAB (Computer Software) http://sdetoolbox.sourceforge.net/

[43] Daqaq M F 2012 On intentional introduction of stiffness nonlinearities for energy harvesting under white gaussian excitations *Nonlinear Dyn.* **69** 1063–79

[44] Harne R L and Dai Q 2017 Characterizing the robustness and susceptibility of steady-state dynamics in post-buckled structures to stochastic perturbations *J. Sound Vib.* **395** 258–71

[45] Daqaq M F 2011 Transduction of a bistable inductive generator driven by white and exponentially correlated Gaussian noise *J. Sound Vib.* **330** 2554–64

[46] Masana R and Daqaq M F 2013 Response of duffing-type harvesters to band-limited noise *J. Sound Vib.* **332** 6755–67

[47] Cottone F, Vocca H and Gammaitoni L 2009 Nonlinear energy harvesting *Phys. Rev. Lett.* **102** 080601

Corrigendum: Energy capture and storage in asymmetrically multistable modular structures inspired by skeletal muscle (2017 Smart Mater. Struct. 26 085011)

Narayanan Kidambi[1], Ryan L Harne[2] and K W Wang[1]

[1] Department of Mechanical Engineering, University of Michigan, Ann Arbor, MI, United States of America 48109
[2] Department of Mechanical and Aerospace Engineering, The Ohio State University, Columbus, OH, United States of America 43210

E-mail: kidambi@umich.edu
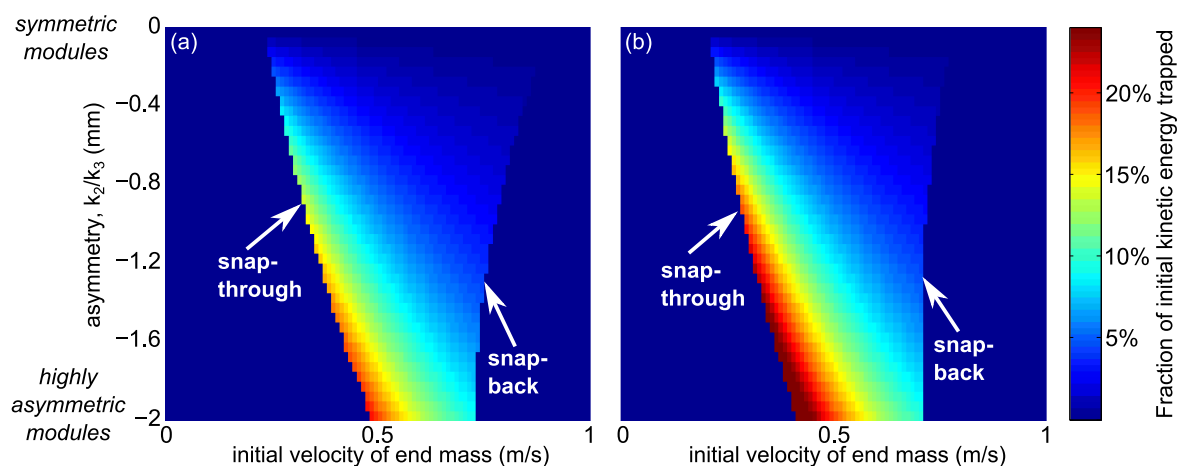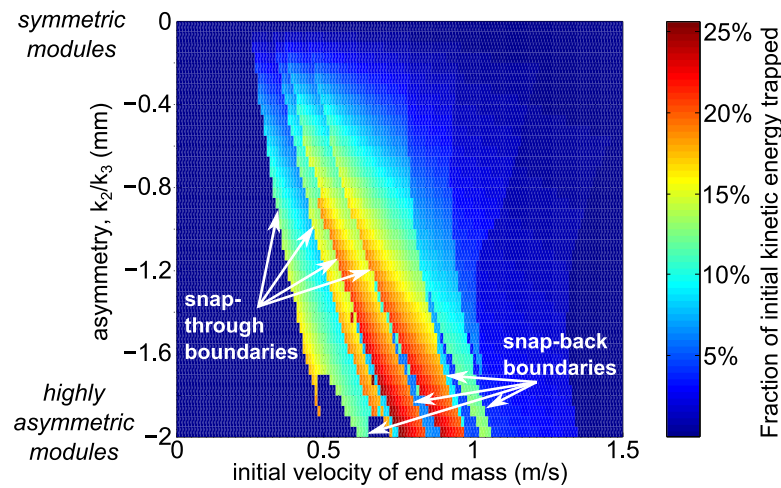
CrossMark

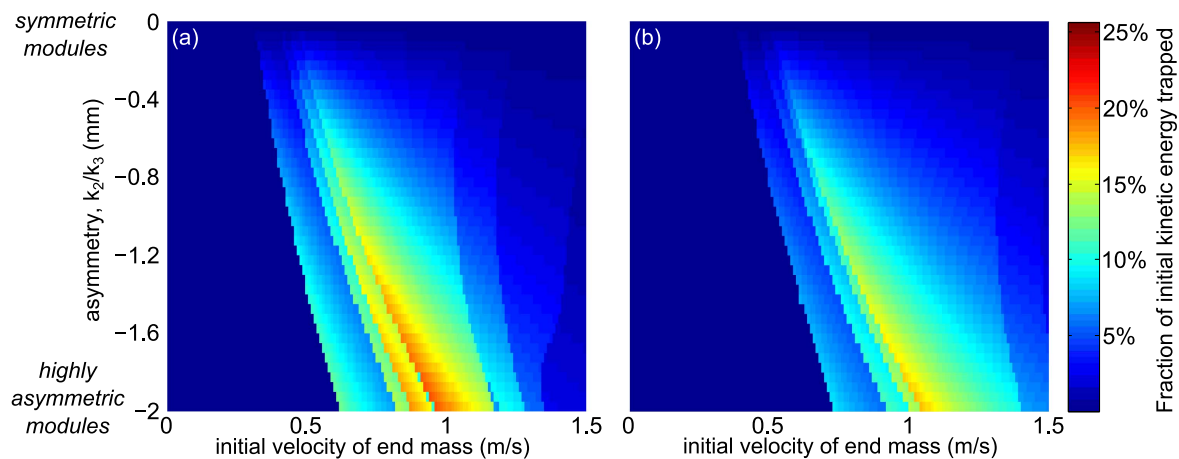(Some figures may appear in colour only in the online journal)

This corrigendum presents figures 16–19 in the final version of the article redrawn to address clarity and readability. The authors regret any inconvenience this may have caused.

Figure 16. (a) Analytical prediction and (b) numerical simulation of fraction of initial kinetic energy T_0 from an impulsive excitation trapped as recoverable strain energy as level of asymmetry is varied under a range of initial velocities. Linear and cubic stiffness terms k_1 and k_3 are obtained from the cubic nonlinear approximation to the experimentally-obtained force-displacement profile shown in figure 6 for the module with 2% beam curvature. The quadratic stiffness k_2 is varied along the vertical axis to tailor the asymmetry. Boundaries demarcating the onset of snap-through and snap-back are clearly visible.
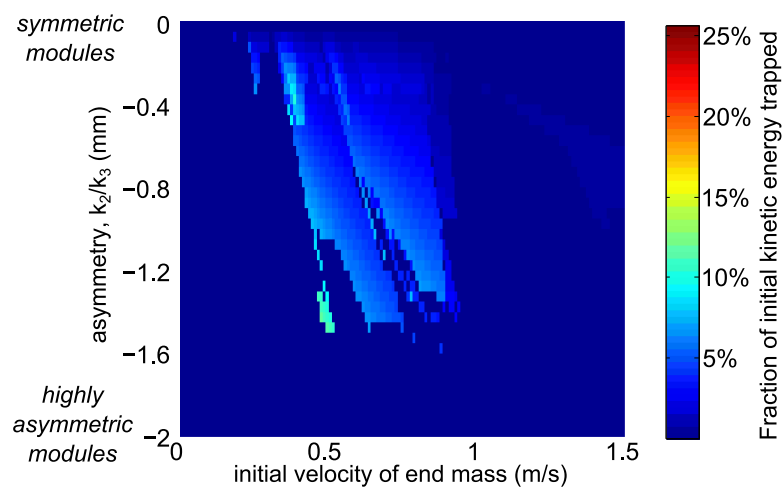
Figure 17. Fraction of initial kinetic energy T_0 that is trapped as recoverable elastic potential energy by the structure as the level of asymmetry and initial velocity of the end mass are varied. Linear and cubic stiffness parameters are obtained from a least-squares fit of a cubic nonlinear stiffness to the experimentally-obtained force-displacement profile of a module with 2% beam curvature. Damping coefficients are selected such that each module's linearized damping ratio is $\zeta = 0.4$ at the low-energy configuration. The discrete boundaries of energy trapping performance indicate the occurrence of snap-through and snap-back. Greatest energy trapping performance is observed at high asymmetry levels, but this comes with an increased risk of snap-back.

Figure 18. Fraction of initial kinetic energy T_0 that is trapped as recoverable elastic potential energy by the structure as the level of asymmetry and initial velocity of the end mass are varied when damping coefficients are selected such that the linearized damping ratios are (a) $\zeta = 0.6$ and (b) $\zeta = 0.8$ in the low-energy configurations. Compared with the results for $\zeta = 0.4$ in figure 17, larger damping ratios generally degrade energy trapping performance, but result in a reduced risk of snap-back at higher asymmetry levels. The portion of initial kinetic energy that is not captured must be dissipated, so the compromised energy trapping performance at higher levels of damping corresponds to a greater proportion of dissipated energy.

Figure 19. Energy trapping performance of a four-module structure for different levels of asymmetry and under various initial velocities v_0. The system's modules are also subject to white noise excitation with $\sigma = 3\,\frac{\text{mm}}{\text{s}^2}$. The presence of noise compromises energy trapping at large levels of asymmetry.